



Title	Radiation-induced segregation and corrosion behavior on Sigma 3 coincidence site lattice and random grain boundaries in proton-irradiated type-316L austenitic stainless steel
Author(s)	Sakaguchi, N.; Endo, M.; Watanabe, S.; Kinoshita, H.; Yamashita, S.; Kokawa, H.
Citation	Journal of Nuclear Materials, 434(1-3), 65-71 https://doi.org/10.1016/j.jnucmat.2012.11.036
Issue Date	2013-03
Doc URL	http://hdl.handle.net/2115/52689
Type	article (author version)
File Information	JNM-D-12-00533.pdf



[Instructions for use](#)

Radiation-induced segregation and corrosion behavior on $\Sigma 3$ coincidence site lattice and random grain boundaries in proton-irradiated type-316L austenitic stainless steel

N. Sakaguchi ^{a,*}, M. Endo ^a, S. Watanabe ^a, H. Kinoshita ^b, S. Yamashita ^c, H. Kokawa ^d

^a *Center for Advanced Research of Energy and Materials, Faculty of Engineering, Hokkaido*

University, Sapporo 060-8628, Hokkaido, Japan

^b *Fukushima National College of Technology, Iwaki 970-8034, Fukushima, Japan*

^c *Fuels and Materials Department, O-arai Research and Development Center, Japan Atomic Energy*

Agency, Ibaraki 311-1393, Japan

^d *Graduate School of Engineering, Tohoku University, Sendai 980-8579, Japan*

*Corresponding Author

Tel: +81-011-706-6768, Fax: +81-011-706-6768

E-mail: sakaguchi@eng.hokudai.ac.jp

Present address: Center for Advanced Research of Energy and Materials, Faculty of Engineering, Hokkaido University, Kita-13, Nishi-8, Kita-ku, Sapporo 060-8628, Hokkaido, Japan

Abstract

The behavior of radiation-induced segregation (RIS) and intergranular corrosion at random grain boundaries and $\Sigma 3$ coincidence site lattice (CSL) boundaries in proton-irradiated 316L stainless steel was examined. The frequency of the CSL boundaries was enhanced up to 86.6 % by grain boundary engineering treatment prior to irradiation. Significant nickel enrichment and chromium depletion were induced at the random grain boundary owing to the RIS. At faceted $\Sigma 3$ CSL boundaries, chromium depletion occurred at the asymmetrical boundary facet plane whereas no RIS was observed at the coherent twin boundary. After the electrochemical etching test, an intergranular corrosion groove was found along the random grain boundaries because of the low chromium concentration (~12 %) at the boundaries. At the faceted $\Sigma 3$ CSL boundaries, the discontinuous groove along the asymmetric facet plane was completely disrupted by the non-corrosive coherent twin boundary.

Keywords

Grain boundary engineering, coincidence site lattice, proton irradiation, radiation-induced segregation, intergranular corrosion

1. Introduction

Solute redistribution in concentrated alloys under irradiation results from the preferential interaction between the solute atoms and excess point defects migrating toward sinks, such as dislocations, surfaces and grain boundaries [1–3]. In austenitic stainless steels, which are used as core materials for the boiling water reactor (BWR) and pressurized water reactor (PWR), radiation-induced segregation (RIS) near the grain boundaries degrades their mechanical and chemical properties significantly [4–7]. The gravity of this problem has been considered as irradiation-assisted stress corrosion cracking (IASCC) caused by the RIS because of the depletion of the chromium concentration near the grain boundaries [8–10]. Recently, the correlation between the RIS and nature of the grain boundaries has been studied for proton- [11] and electron-irradiated [12] austenitic stainless steels. It has been indicated that the magnitude of the RIS depends upon the grain boundary type: significant RIS occurred at random (general) grain boundaries whereas the RIS was suppressed visibly at coincidence site lattice (CSL) boundaries. The relationship between the grain boundary nature and crack initiation by intergranular stress corrosion cracking (IGSCC) has also been discussed by West and Was [13]. They realized that the low angle and $\Sigma 3$ CSL boundaries were less susceptible to IGSCC than random grain boundaries in a supercritical water environment.

Regarding localized corrosion on the grain boundaries, many studies have clarified that the susceptibility of grain boundary corrosion depends strongly on the nature of the grain boundary

[14–16]. In general, low angle and CSL boundaries are classified by low energy boundaries while other high angle boundaries are termed random grain boundaries with high boundary energy. It is accepted that the low energy boundaries are highly resistant to intergranular corrosion. Accordingly, grain boundary engineering (GBE) processing has been developed [17–19] to improve significantly the material properties without changing the alloy composition or adding minor elements. Moreover, improvements in the grain boundary corrosion property can also be achieved in the austenitic stainless steels prepared using the GBE treatments [19].

In this study, we have investigated the behavior of RIS and intergranular corrosion on random grain boundaries and $\Sigma 3$ CSL boundaries in 316L austenitic stainless steel after proton irradiation. A correlation among the RIS, corrosion property and grain boundary nature was established by transmission electron microscopy (TEM) and electrochemical etching. Availability of the GBE treatment for intergranular corrosion during irradiation will be discussed.

2. Experimental procedure

2.1 Sample preparation

The composition of the type-316L austenitic stainless steel is given in Table 1. The procedure of GBE for the 316L stainless steel was as follows. As-received 316L stainless steel was solution-annealed at 1373 K for 30 minutes. The sample was then subjected to 1 % cold rolling and

finally was annealed again at 1260 K for 72 hours to increase the frequency of the CSL boundaries to over 80 %. Electron backscatter diffraction (EBSD) patterns were acquired using a scanning electron microscope (SEM; Philips XL-3) equipped with an EBSD instrument to confirm the CSL boundary frequency in the GBE sample. The sample was then polished mechanically to a thickness of 0.15 mm. The foil sample was punched out onto TEM disks of 3 mm diameter and electropolished in a 5 % HClO₄ + 95 % CH₃COOH solution.

2.2 Proton irradiation

Proton irradiation was carried out for the foil sample using a multi-beam high-voltage electron microscope (MBHVEM; JEOL JEM-ARM-1300) equipped with 300 and 400 kV ion accelerators. The H⁺ ions with acceleration energies of 280 kV were irradiated at a dose of 2.7×10^{17} ions/cm² at 673 K. The damage profile calculated by SRIM software [20] is shown in Fig. 1. The average irradiation dose was 0.2 dpa at a depth of 250 nm.

2.3 TEM observations

After proton irradiation, the chemical compositions near random grain boundaries and $\Sigma 3$ CSL boundaries were analyzed using a field-emission gun TEM (FEG-TEM; JEOL JEM-2010F) equipped with an energy-dispersive X-ray spectroscope (NORAN Inc. VOYAGER). After EDS analysis, the sample was etched electrochemically in 10 % oxalic acid solution at a current density of 0.07 A/cm² for 1 minute. The sample was then inserted into the FEG-TEM and energy-filtered TEM

(EF-TEM) images were acquired by Gatan Imaging Filter (Gatan Inc. Model 678) to reveal the mass loss at the grain boundaries after etching.

3. Results and discussion

The grain boundary character distribution obtained by SEM-EBSD analysis of as-received and GBE 316L stainless steels is presented in Fig. 2. The black and gray lines indicate the random grain boundaries and CSL boundaries ($\Sigma \leq 29$), respectively. Prior to the GBE treatment, the frequency of the CSL boundaries was measured to be 64.2 % in the as-received 316L. The frequency of the CSL boundaries in the GBE 316L was increased significantly to 86.6 % and a network of random grain boundaries was divided perfectly by the CSL boundaries. This is a common feature among the GBE materials which show high resistivity for material degradation along the grain boundaries. Here, the ratio of each CSL boundary in the usual GBE austenitic stainless steel is 75 % for the $\Sigma 3$ CSL boundary, 10 % for the $\Sigma 9$ CSL boundary and 15 % for the other CSL boundaries. This is the reason for us addressing the behavior on the $\Sigma 3$ CSL boundaries. Additionally, the solute concentration profiles across the grain boundaries in the GBE 316L were measured by the TEM/EDX as shown in Fig. 3. No visible segregation was detected on the random grain boundaries and twin boundaries.

A typical microstructure of the proton-irradiated GBE sample is shown in Fig. 4(a). A random grain boundary was stubbed by a $\{111\}$ $\Sigma 3$ CSL boundary (coherent twin boundary) indicated by the

yellow arrow. The measured solute concentration profiles across the random grain boundary and coherent twin boundary are shown in Fig. 4(b) and (c), respectively. Remarkable nickel enrichment and chromium depletion owing to the RIS occurred on the random grain boundary. Particularly, the concentration of the chromium was less than 12 mass % at and near the grain boundary. The RIS of the minor elements (silicon enrichment and molybdenum depletion) was also indicated at the grain boundary. Conversely, no RIS was observed on the coherent twin boundary because of its low sink strength as described in [21].

Almost all of the $\Sigma 3$ CSL boundaries can be faceted into two individual boundaries. The faceted $\Sigma 3$ CSL boundary is always altered into a pair of the twin boundary and another asymmetric $\Sigma 3$ CSL boundary as shown in Fig. 5(a). The solute concentration profiles across the asymmetric $\Sigma 3$ CSL boundary and the coherent twin boundary are shown in Fig. 5(b) and (c), respectively. Similarly in the above mentioned, no RIS was induced near the coherent twin boundary, whereas remarkable compositional changes were seen at the asymmetric $\Sigma 3$ CSL boundary. The chromium concentration at the asymmetric boundary was approximately 11 mass %, which was the same level as that at the random grain boundary. This indicates that the asymmetric $\Sigma 3$ CSL boundary is not classified to a low energy boundary anymore; it should have a much higher grain boundary energy than that in the coherent twin boundary. The matching or indices of the boundary planes is therefore one of the important parameters, as for the Σ value, describing the nature of the grain boundary. In fact, it has

been reported by experimental [22] and theoretical approaches [23] that the boundary energy of the $\{111\}$ $\Sigma 3$ CSL (coherent twin) is always lower than that of the $\{112\}$ $\Sigma 3$ CSL (incoherent twin) and other CSL boundaries in face-centered cubic (FCC) metals. Thus, the asymmetric $\Sigma 3$ CSL boundaries are classified to a high energy boundary, which acts as a strong sink site for the point defects.

To clarify the relationship between the RIS and intergranular corrosion at the random and $\Sigma 3$ CSL boundaries, the electrochemical etching test was applied to the unirradiated and proton-irradiated samples. The microstructure of a region including the interconnection of a random grain boundary and coherent twin boundaries in unirradiated GBE316L after the electrochemical etching is shown in Fig. 6. As shown in the TEM micrograph and the EF-TEM analysis, any visible selective etching on the grain boundary was not seen in both the random grain boundary and twin boundaries in the present etching condition. A similar microstructure of the proton-irradiated sample after the electrochemical etching is shown in Fig. 7(a). Unlike a previous result, it is very obvious that the random grain boundary was corroded by the etching test while no structural change was observed at the twin boundary. The EF-TEM image was then acquired to estimate the thickness changes at the grain boundary. A thickness map near the random grain boundary and corresponding thickness profile across the grain boundary are given in Fig. 7(b) and (c), respectively. Since a thicker region appears as a brighter contrast in the thickness map, it is shown clearly that the intergranular

corrosion groove along the grain boundary was formed by the etching. In the thickness profile, the depth and the width of the groove were measured to be approximately 40 and 10 nm, respectively. The measured width of the groove was almost equal to the width of the RIS at a typical random grain boundary, as shown in Fig. 4(b). This implies that the intergranular corrosion is caused by chromium depletion along the grain boundary. In fact, we could never find this type of grooving in the unirradiated sample. Similarly, no groove is observed along the twin boundary because the RIS never occurs there.

The corrosion behavior along the faceted $\Sigma 3$ CSL boundary was also investigated as shown in Fig. 8. The evident intergranular corrosion groove appeared along the asymmetric $\Sigma 3$ CSL boundary with the same depth and width levels as those in the random grain boundary, however, the groove appeared to be discontinuous at several places. In these regions, the non-corroded coherent twin boundaries have always existed between two separated grooves. The length of the coherent twin boundary shown in Fig. 8 was approximately 50 nm, which is two or three times larger than the RIS width at the asymmetric $\Sigma 3$ CSL boundaries. This result is not in conflict with the RIS behavior on the faceted $\Sigma 3$ CSL boundary as shown in Fig. 5. It is therefore expected that the penetration of the corrosion along the $\Sigma 3$ CSL boundary will be stopped perfectly when the corrosive asymmetric $\Sigma 3$ CSL boundaries meet the non-corrosive coherent twin boundary. In other words, a faceted $\Sigma 3$ CSL boundary effectively prevents corrosion penetration although localized corrosion will be generated

on the one boundary facet plane with an asymmetrical structure.

In Fig. 9(a), we show a panoramic TEM photograph of the proton-irradiated 316L sample after the electrochemical etching test. Some grain boundaries were attacked preferentially because of the chromium depletion caused by the RIS. The interconnections of the corroded and non-corroded grain boundaries are indicated by the green arrows in the photograph and a schematic illustration of the grain boundary network is shown in Fig. 9(b). As predicted from the previous result, the corrosive network along the grain boundaries is disrupted completely by the non-corrosive grain boundaries such as the coherent twin. Although the evaluation of the corrosive network in our study is limited only to the sample surface, it is expected that the network of random grain boundaries is divided perfectly in 3-dimensions by the CSL boundaries in the GBE materials with a CSL frequency of 80 % [24]. Thus, the corrosion propagation through a corrosive network caused by the RIS at grain boundaries would be prevented effectively in the GBE austenitic stainless steels. This will be one of the essential features for the prevention of the IASCC in the BWR and PWR environment. Further experiments with neutron irradiation will be required to confirm the above speculation. This will also help us to understand the effect of the CLS boundaries on crack prevention.

4. Conclusion

By the GBE thermomechanical treatment, the frequency of the CSL boundaries in the 316L

austenitic stainless steel increased from 64.2 % to 86.6 %. Nickel enrichment and chromium depletion owing to the RIS were induced at random grain boundaries and asymmetric $\Sigma 3$ CSL boundaries by proton irradiation, whereas no RIS occurred at the $\{111\}$ $\Sigma 3$ CSL (coherent twin) boundary. After the etching test, intergranular corrosion grooves were present along the random and asymmetric $\Sigma 3$ CSL boundaries where the chromium concentration was lower than 12 %. At the faceted $\Sigma 3$ CSL boundaries, the discontinuous groove along the asymmetric facet plane was disrupted completely by the non-corrosive coherent twin boundary, thus the faceted $\Sigma 3$ CSL boundary would effectively prevent corrosion penetration. It is concluded that the corrosion propagation through a corrosive network caused by the RIS at grain boundaries would be prevented effectively in GBE austenitic stainless steel having high dense CSL boundaries.

Acknowledgements

The authors gratefully thank Mr. K. Sugawara and Mr. K. Ohkubo for their technical support in the MBHVEM operations.

References

- [1] R.A. Johnson, N.Q. Lam, Phys. Rev. B 13 (1976) 4364–4375.
- [2] S. Watanabe, N. Sakaguchi, N. Hashimoto, H. Takahashi, J. Nucl. Mater. 224 (1995) 158–168.

- [3] A. Etienne, B. Radiguet, N.J. Cunningham, G.R. Odette, P. Pareige, *J. Nucl. Mater.* 406 (2010) 244–250.
- [4] R. Katsura, M. Kodama, S. Nishimura, *Corrosion* 48 (1992) 384–390.
- [5] S.M. Bruemmer, E.P. Simonen, P.M. Scott, P.L. Andresen, G.S. Was, J.L. Nelson, *J. Nucl. Mater.* 274 (1999) 299–314.
- [6] C.R. Arganis-Juarez, J.M. Malob, J. Uruchurtu, *Nucl. Eng. Des.* 237 (2007) 2283–2291.
- [7] K. Fukuya, K. Fujii, H. Nishioka, K. Takakura, K. Nakata, *Nucl. Eng. Des.* 240 (2010) 473–481.
- [8] S.M. Bruemmer, E.P. Simonen, *Corrosion* 50 (1994) 940–946.
- [9] J.T. Busby, G.S. Was, E.A. Kenik, *J. Nucl. Mater.* 302 (2002) 20–40.
- [10] S. Teyseyre, Z. Jiao, E. West, G.S. Was, *J. Nucl. Mater.* 371 (2007) 107–117.
- [11] T.S. Duh, J.J. Kai, F.R. Chen, *J. Nucl. Mater.* 283–287 (2000) 198–204.
- [12] S. Watanabe, Y. Takamatsu, N. Sakaguchi, H. Takahashi, *J. Nucl. Mater.* 283–287 (2000) 152–156.
- [13] E.A. West, G.S. Was, *J. Nucl. Mater.* 392 (2009) 264–271.
- [14] X.R. Qian, Y. Chou, *Phil. Mag. A* 45 (1982) 1075–1079.
- [15] G. Palumbo, K.T. Aust, *Acta Metall. Mater.* 38 (1990) 2343–2352.
- [16] H. Kokawa, M. Shimada, Y.S. Sato, *JOM* 52 (2000) 34–37.
- [17] C. Cheung, U. Erb, G. Palumbo, *Mater. Sci. Eng., A* 185 (1994) 39–43.

[18] S. Spigarelli, M. Cabibbo, E. Evangelista, G. Palumbo, *Mater. Sci. Eng., A.* 352 (2003) 93–99.

[19] M. Michiuchi, H. Kokawa, Z.J. Wang, Y.S. Sato, K. Sakai, *Acta Mater.* 54 (2006) 5179–5184.

[20] <http://www.srim.org/>

[21] N. Sakaguchi, S. Watanabe, H. Takahashi, R.G. Faulkner, *J. Nucl. Mater.* 329–333 (2004)

1166–1169.

[22] G. Hasson, J.Y. Boos, I. Herbeuval, M. Biscondi, C. Goux, *Surf. Sci.* 31 (1972) 115–137.

[23] J.D. Rittner, D.N. Seidman, *Phys. Rev. B: Condens. Matter Mater. Phys.* 54 (1996) 6999–7015.

[24] M. Frary, C.A. Schuh, *Phil. Mag.* 85 (2005) 1123–1143.

Table captions

Table 1. Bulk composition of 316L austenitic stainless steel in mass percent.

Figure captions

Fig. 1 Calculated damage profile of 280 keV proton irradiation to 2.7×10^{17} ions/cm² as a function of depth.

Fig. 2 Grain boundary character distribution obtained by SEM/EBSD for as-received and grain boundary engineered 316L stainless steels. Black and gray lines indicate random and CSL boundaries ($\Sigma < 29$), respectively.

Fig. 3 Solute concentration profiles in unirradiated 316L stainless steel across (a) random grain boundary and (b) twin boundary.

Fig. 4 (a) TEM micrograph of grain boundary network consisting of random grain boundary and coherent twin boundary in proton-irradiated 316L stainless steel and solute concentration profiles across (b) random grain boundary and (c) twin boundary.

Fig. 5 (a) TEM micrograph of faceted $\Sigma 3$ CSL boundary in proton-irradiated 316L stainless steel and solute concentration profiles across (b) asymmetric $\Sigma 3$ CSL boundary and (c) twin boundary.

Fig. 6 (a) TEM micrograph of random grain boundary and twin boundaries in unirradiated 316L

stainless steel after electrochemical etching, (b) thickness map of random grain boundary acquired by EF-TEM and (c) thickness profile across the boundary..

Fig. 7 (a) TEM micrograph of random grain boundary and twin boundary in proton-irradiated 316L stainless steel after electrochemical etching, (b) thickness map of random grain boundary acquired by EF-TEM and (c) thickness profile across the boundary.

Fig. 8 (a) TEM micrograph of faceted $\Sigma 3$ CSL boundary in proton-irradiated 316L stainless steel after electrochemical etching, (b) thickness map of random grain boundary acquired by EF-TEM and (c) thickness profiles across asymmetric $\Sigma 3$ CSL and twin boundaries.

Fig. 9 (a) Panoramic TEM photograph of proton-irradiated 316L stainless steel after electrochemical etching test and (b) schematic illustration of grain boundary network.

Table 1

	C	Si	Mn	P	S	Ni	Cr	Mo	Fe
mass%	0.01	0.59	0.78	0.033	0.001	12.16	17.22	2.06	Bal.

Figure 1

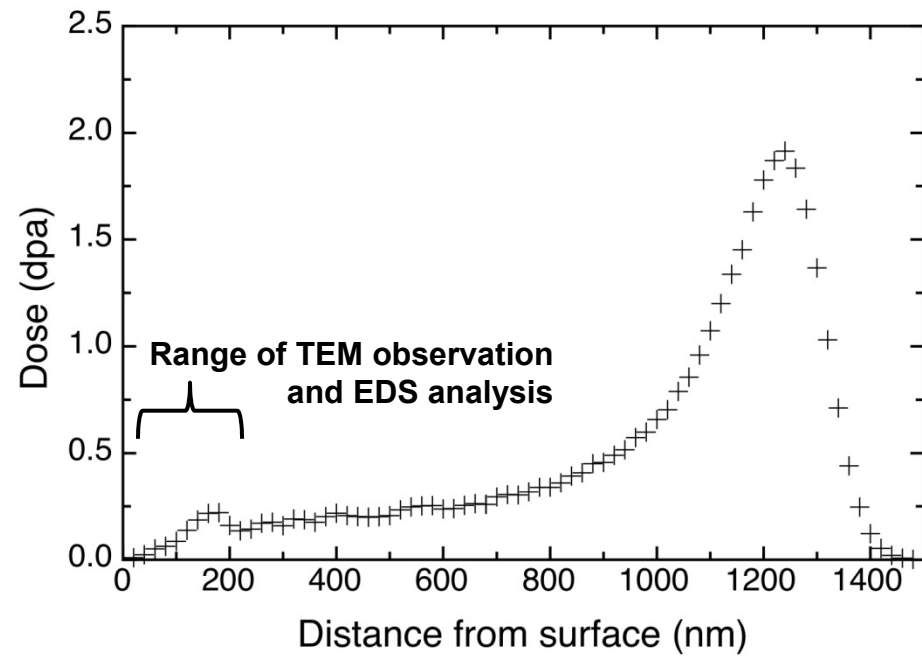
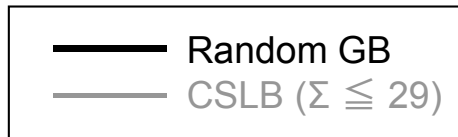
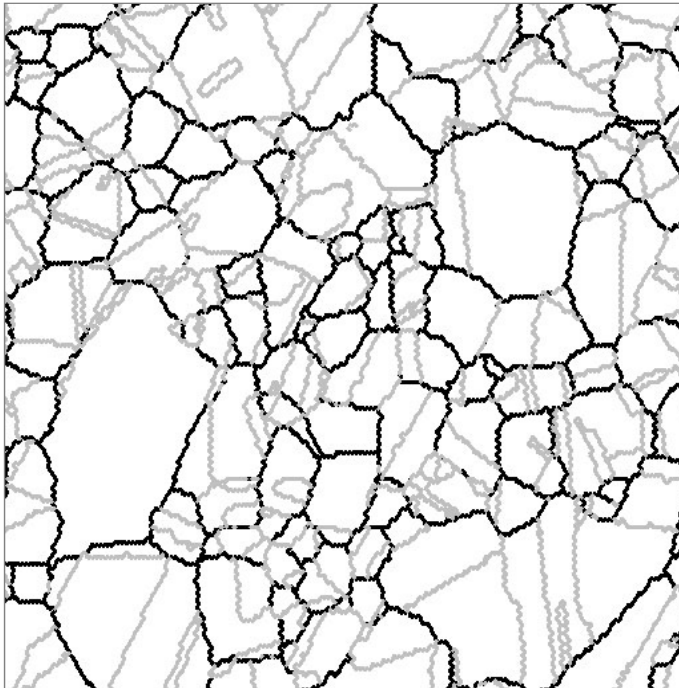


Figure 2

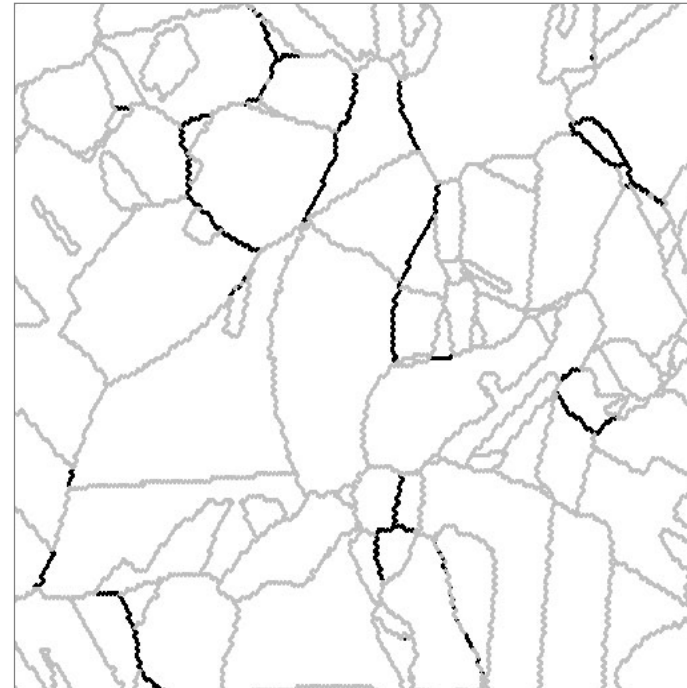


as received 316L



CSLB ratio: 64.2%

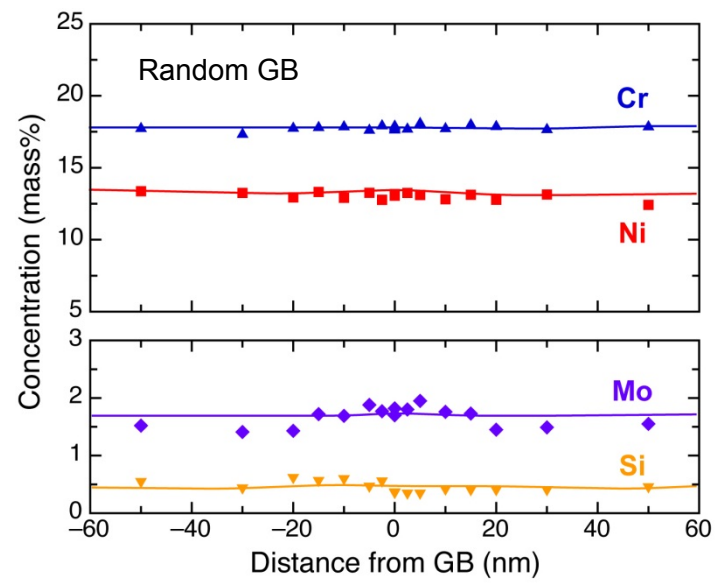
grain boundary engineered 316L



CSLB ratio: 86.6%

Figure 3

(a)



(b)

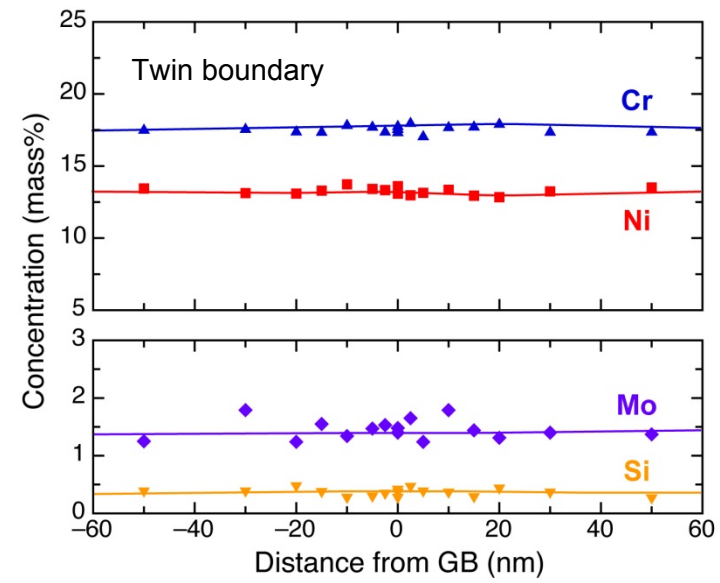
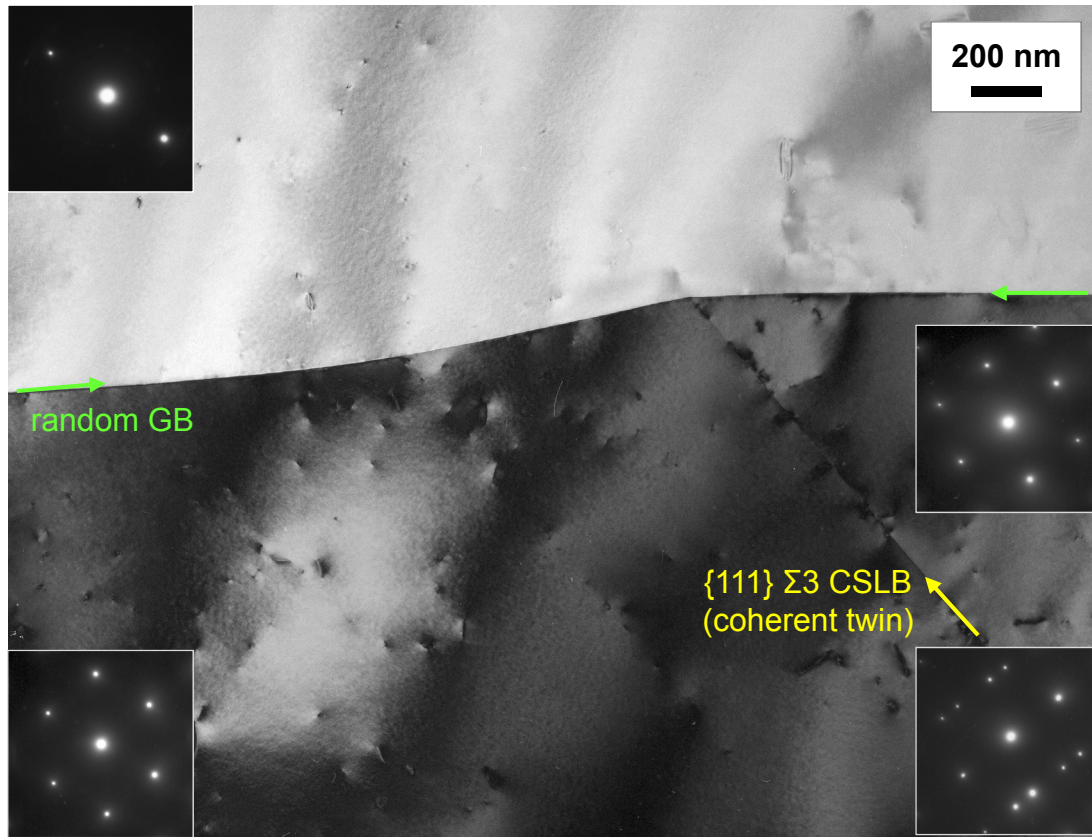


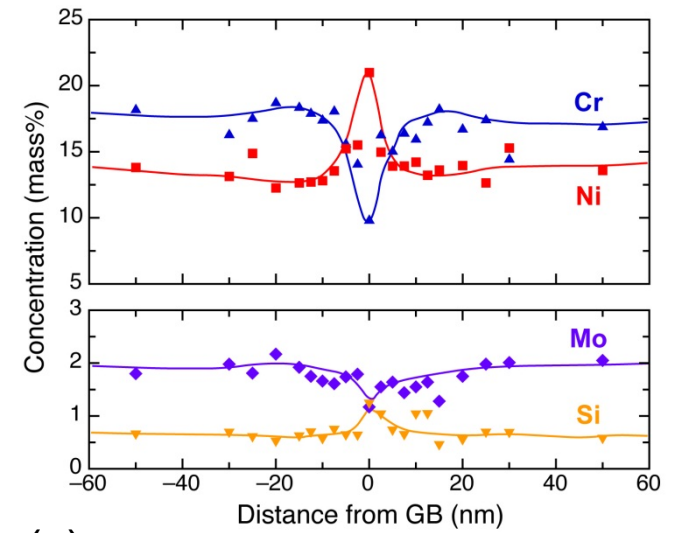
Figure 4

(a)



Proton irradiation at 673 K to 0.2 dpa.

(b)



(c)

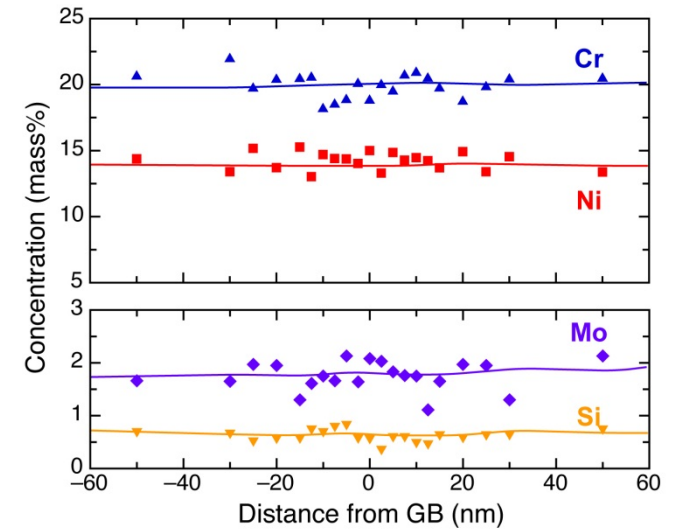
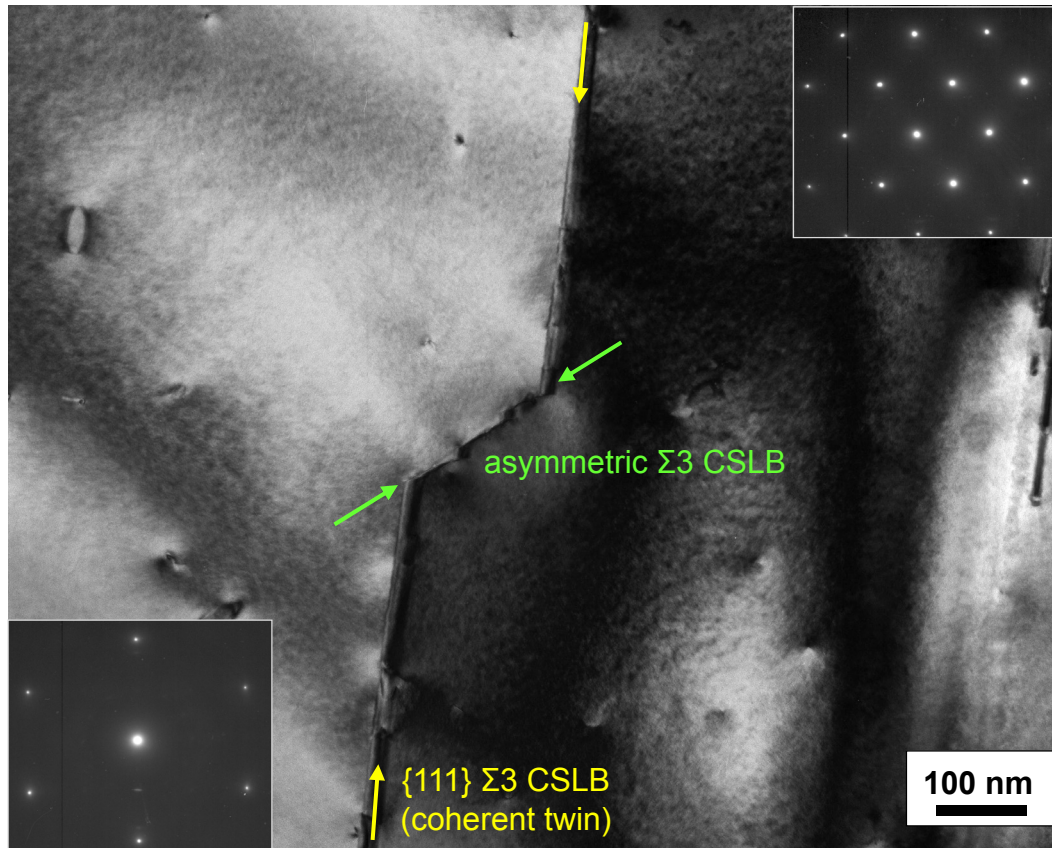


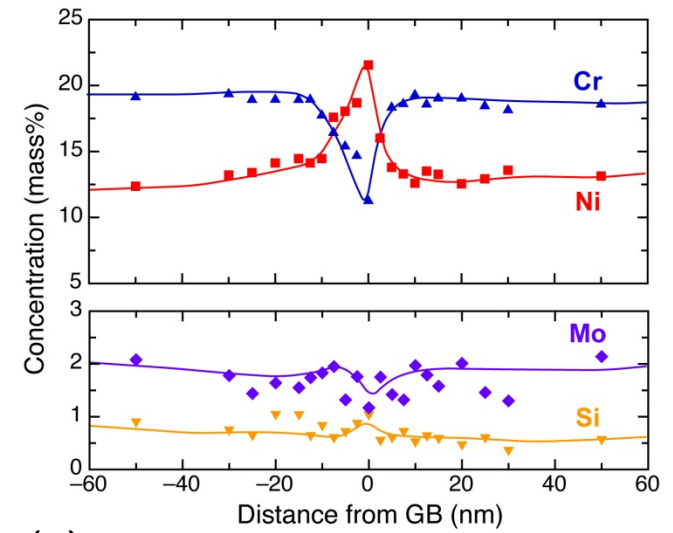
Figure 5

(a)



Proton irradiation at 673 K to 0.2 dpa.

(b)



(c)

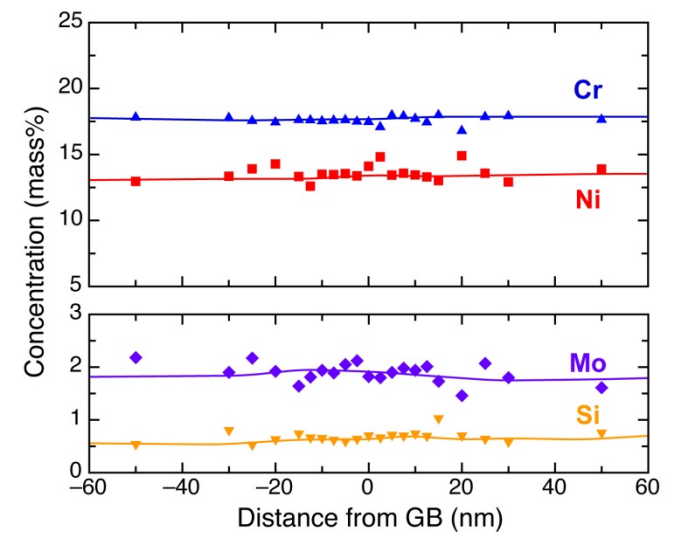
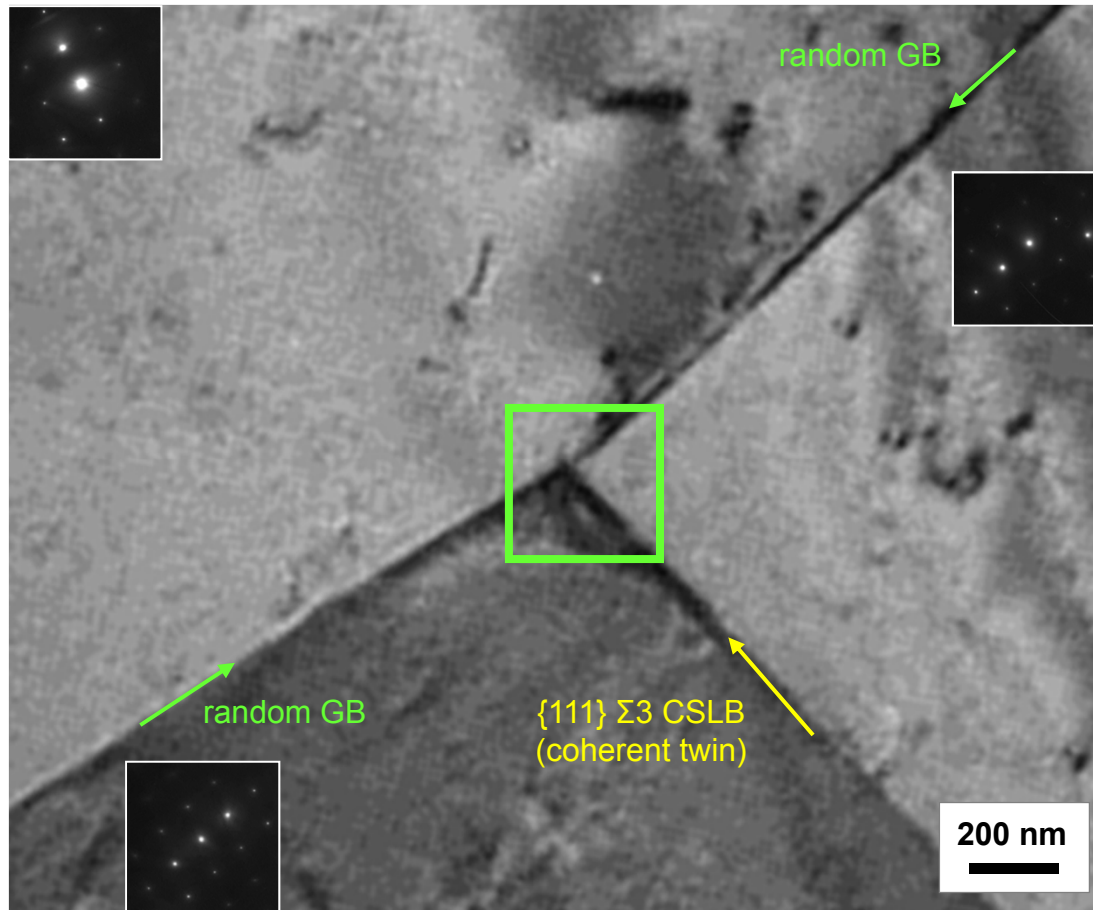
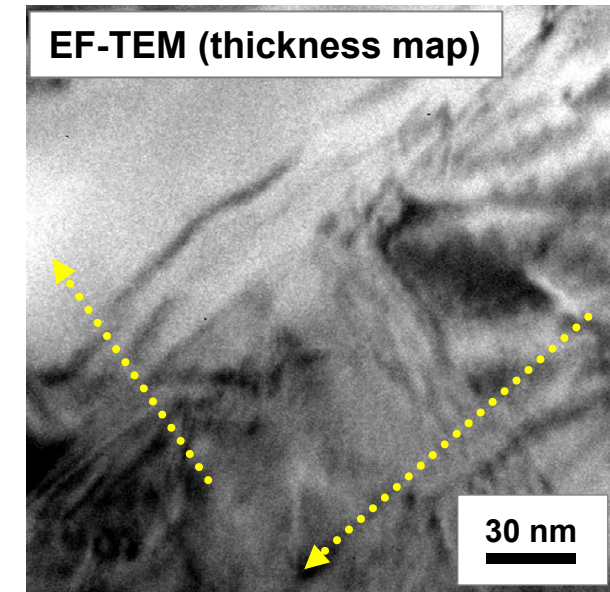


Figure 6

(a)



(b)



(c)

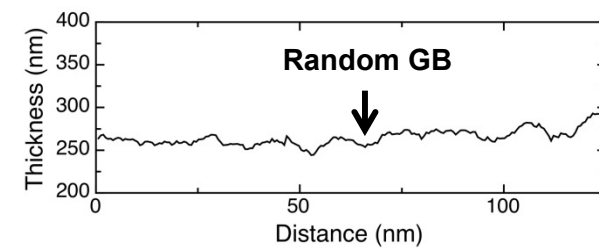
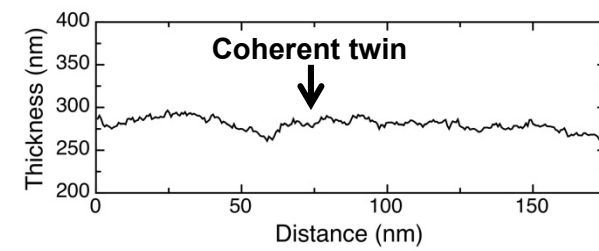
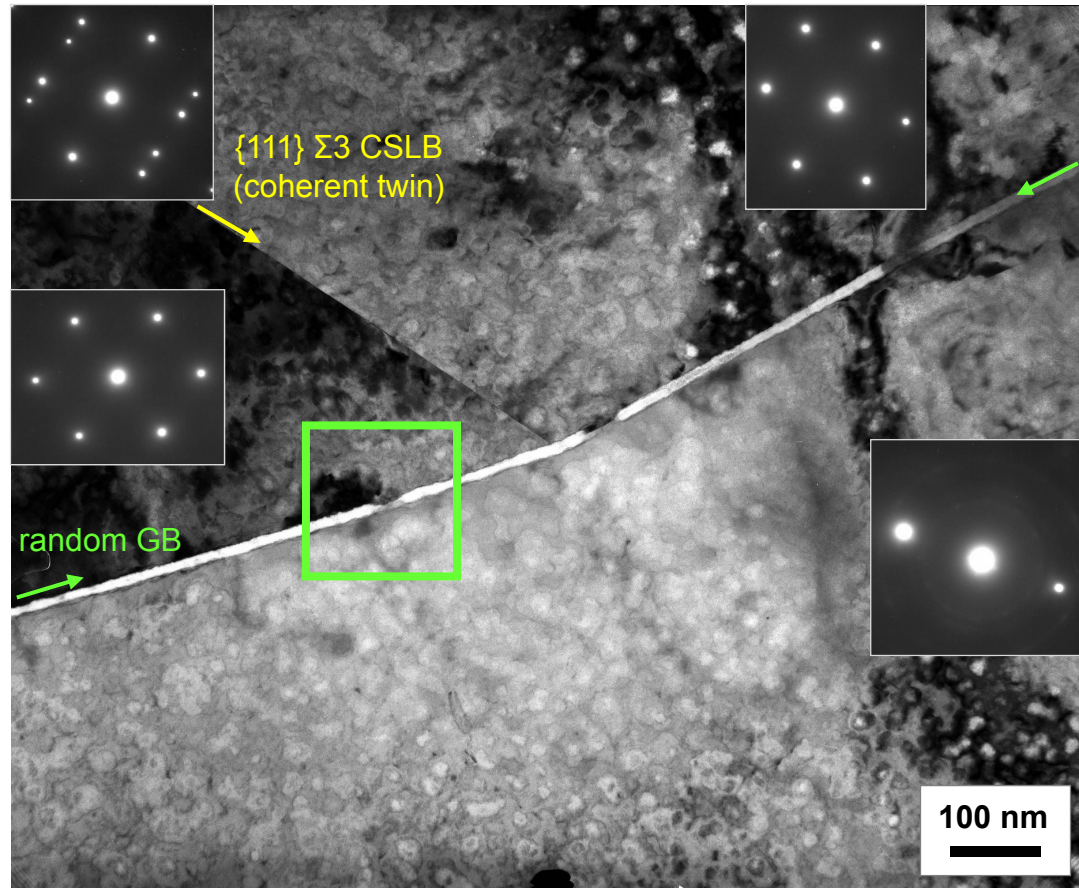
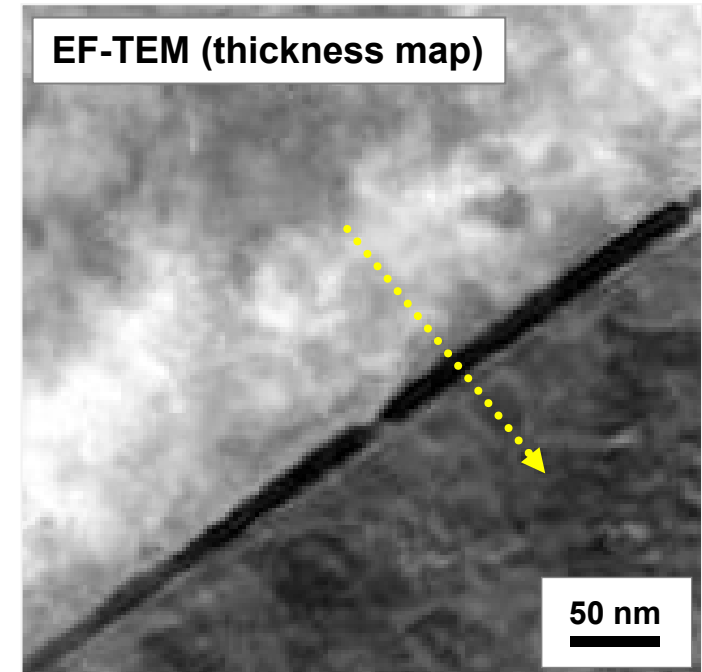


Figure 7

(a)



(b)



(c)

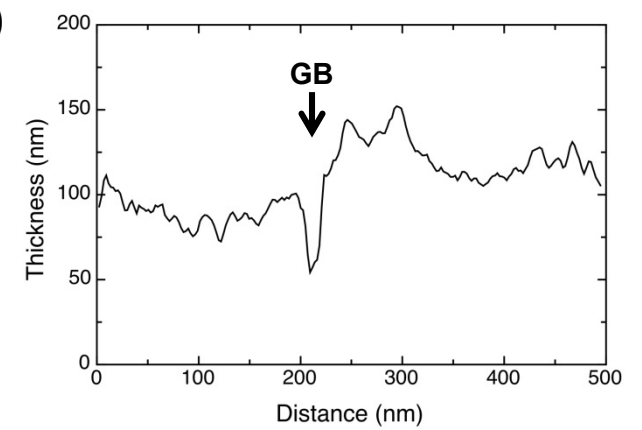
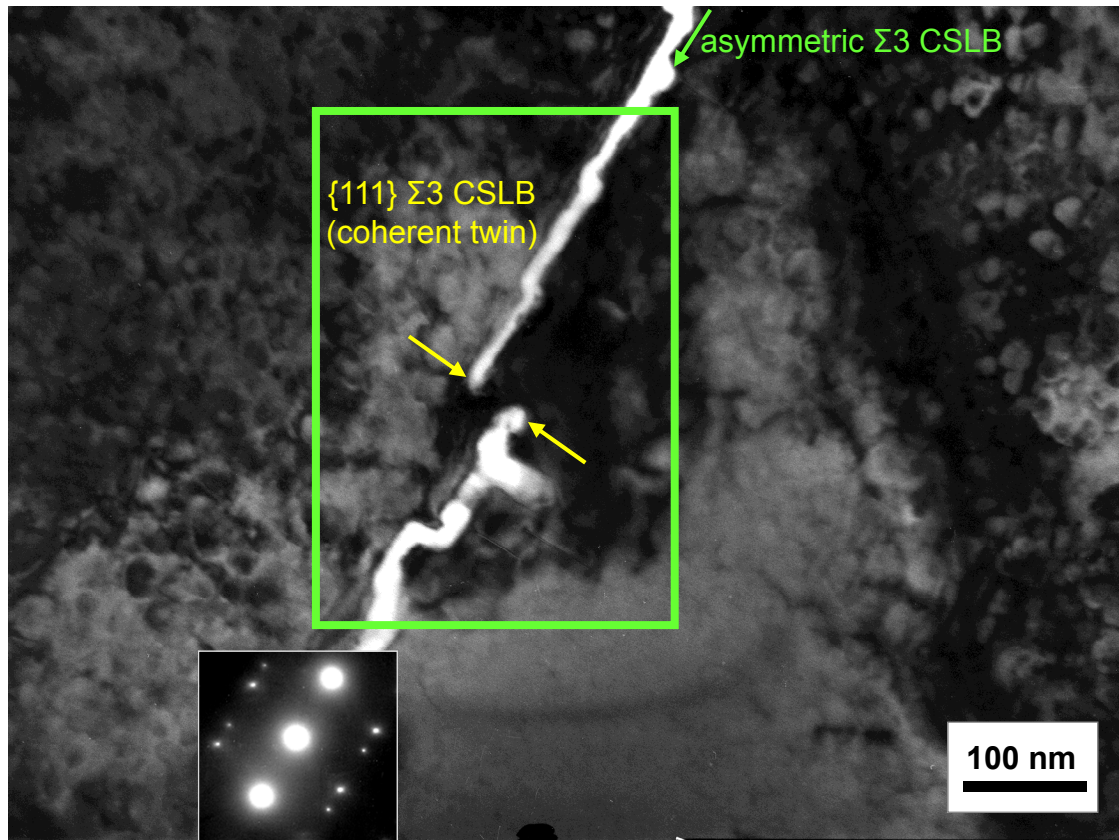
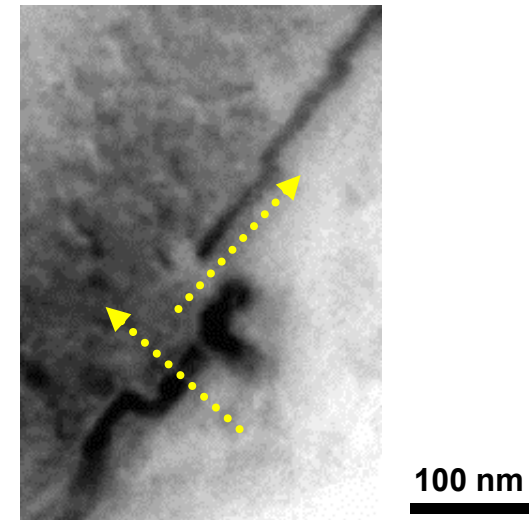


Figure 8

(a)



(b) EF-TEM (thickness map)



(c)

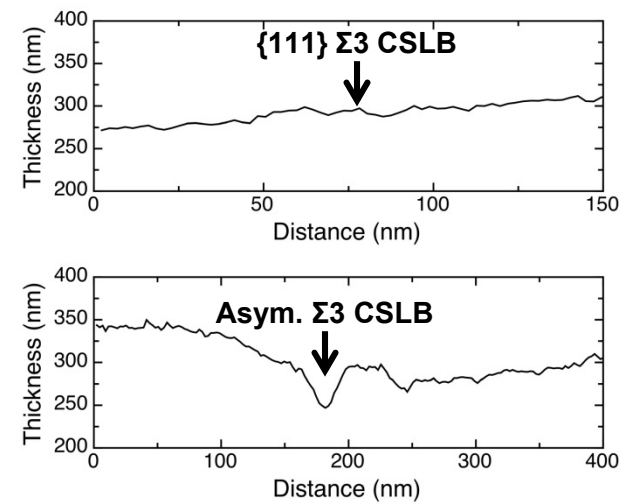
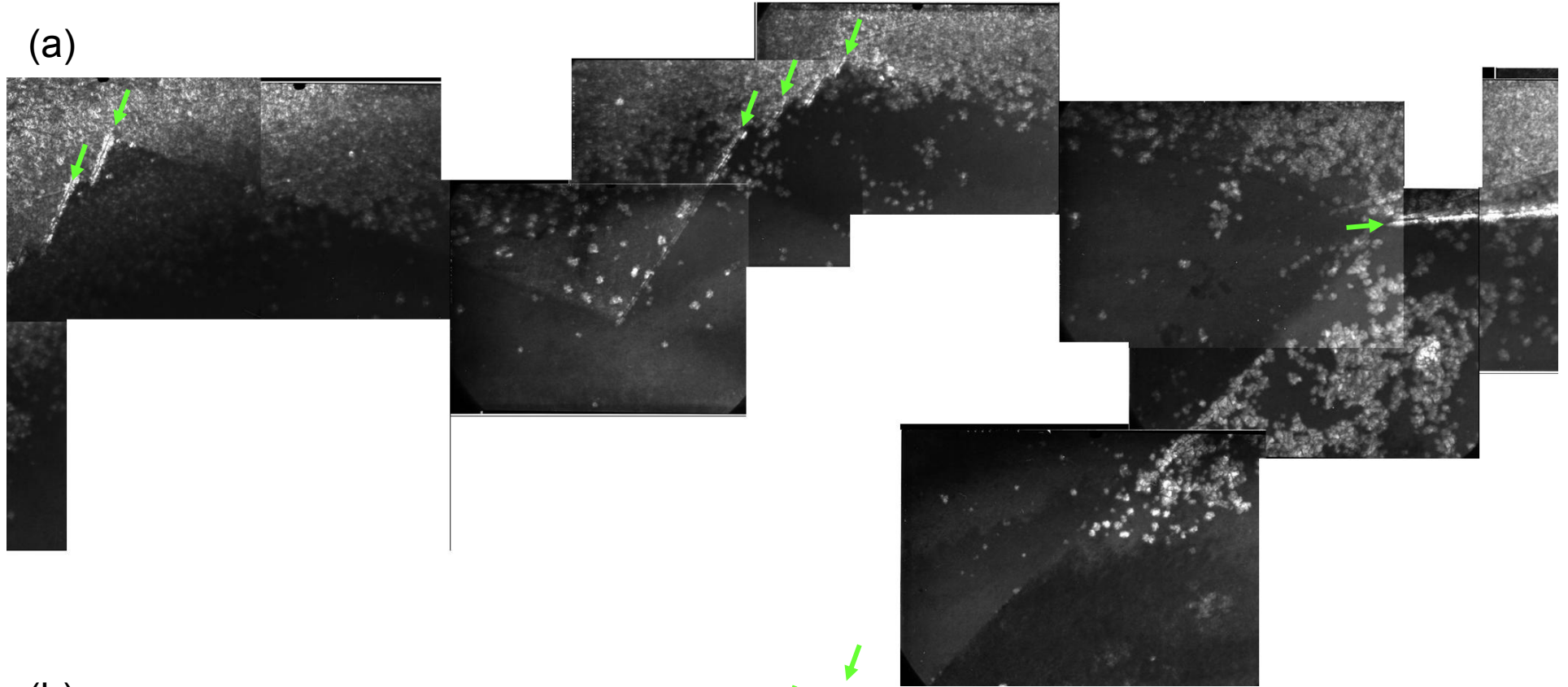


Figure 9

(a)



(b)

